

1 **Creating Patient-Specific Vein Models to Characterize Wall Shear Stress in**  
2 **Hemodialysis Population**

3

4 Andrés Moya-Rodríguez<sup>1,2</sup>, Bingqing Xie<sup>2</sup>, Dylan Cook<sup>2</sup>, Maren Klineberg<sup>3</sup>, Sandeep  
5 Nathan<sup>4</sup>, Mary Hammes<sup>5,†</sup>, Anindita Basu<sup>2,†</sup>

6 <sup>1</sup> Biophysical Sciences Graduate Program, University of Chicago, Chicago, IL, 60637

7 <sup>2</sup> Section of Genetic Medicine, Department of Medicine, University of Chicago, Chicago, IL, 60637

8 <sup>3</sup> College, University of Chicago, Chicago, IL, 60637

9 <sup>4</sup> Section of Cardiology, Department of Medicine, University of Chicago, Chicago, IL, 60637

10 <sup>5</sup> Section of Nephrology, Department of Medicine, University of Chicago, Chicago, IL, 60637

11

12 † Corresponding authors:

13 Anindita Basu, [onibas@uchicago.edu](mailto:onibas@uchicago.edu); Mary Hammes, [mhammes@medicine.bsd.uchicago.edu](mailto:mhammes@medicine.bsd.uchicago.edu)

14

15 **Abstract**

16 End-Stage Renal Disease (ESRD) patients require arteriovenous fistulas (AVF)  
17 that allow a mature vein to withstand hemodialysis. Unfortunately, venous thrombosis and  
18 stenosis in the cephalic vein arch after AVF placement is common and heavily influenced  
19 by hemodynamics. To better assess forces and flow behavior in the cephalic arch, we  
20 have built patient-specific millifluidic models that allow us to explore the complex interplay  
21 between patient-specific vein geometry and fluctuating hemodynamics. These 3D models  
22 were created from patient-specific intravascular ultrasound and venogram images  
23 obtained three- and twelve-months post AVF creation and fabricated into soft elastomer-  
24 based millifluidic devices. Geometric validation of fabricated phantom millifluidic device  
25 shows successful replication of original computational 3D model. Millifluidic devices were  
26 perfused with a blood-mimicking fluid containing fluorescent tracer beads under steady-  
27 state physiologic cephalic vein flow conditions (20 mL/min). Particle image velocimetry  
28 was employed to calculate wall shear stress (WSS) across the cephalic arches.  
29 Experimental WSS profile evaluation reveals that the physiologic cephalic arch model  
30 yields WSS values within physiologic range [76-760 mPa]. Moreover, upon comparing  
31 WSS profiles across all models, it is noticeable that WSS values increase as vein  
32 diameter decreases, which further supports employed experimental and analysis  
33 strategy. The presented millifluidic devices show promise for experimental WSS  
34 characterization under pathologic flow conditions to contrast from calculated physiologic  
35 hemodynamics and better understand WSS influence on thrombosis and stenosis in  
36 hemodialysis patients.

37

38 **1. Introduction**

39         Among the 492,000 patients receiving regular hemodialysis in the United States,  
40 64% (275,000 patients) have an arteriovenous fistula (AVF) for their vascular access [1].  
41 Two thirds of all AVFs placed in the US are in the upper arm using the brachiocephalic  
42 (BCF) configuration, which commonly fails due to cephalic arch stenosis (14-60%) and  
43 thrombosis (17-28%)[2-4]. Failed AVFs lead to missed hemodialysis sessions, which  
44 contributes to the morbidity, mortality and financial burden of interventional procedures  
45 for end-stage renal disease (ESRD) patients [5]. Moreover, our understanding of the  
46 mechanisms of thrombosis in renal failure is incomplete because we lack specific tools to  
47 study thrombosis in AVF clinical scenarios. Traditional anti-platelet and anti-coagulants  
48 do not effectively prevent or treat access thrombosis and can cause significant side  
49 effects [6, 7]. In the absence of reliable clinical predictors of thrombosis, the current  
50 standard of care is to treat AVF thrombosis *a posteriori*. Consequently, there is an urgent  
51 need to define how thrombosis occurs in ESRD downstream from the vascular access in  
52 order to establish effective treatment options or preventative care.

53         We concentrate on the cephalic arch as we posit that its geometric bend has  
54 rheological implications since this is where thrombosis commonly occurs [8]. Vascular  
55 pathogenesis that results in thrombosis and stenosis can be better understood if cephalic  
56 arch geometries and flow conditions are faithfully recreated for extensive *in vitro* studies.  
57 This way, hemodynamics can be dissected in terms of local acting forces which are  
58 intimately tied to vessel geometry, blood viscosity and flow rate. These forces are best  
59 described by wall shear stress (WSS). Although BCF creation initially increases overall  
60 WSS due to dramatically increased blood flow, computational modeling showed that low  
61 WSS develops in the cephalic arch over time [8, 9]. 2D computational fluid dynamics of  
62 the cephalic arch revealed that local WSS in the curved region of the arch can be lower  
63 than the physiologic range [76-760 mPa], which can promote venous stenosis and  
64 thrombosis [10]. We performed a five-year study of an ESRD patient cohort with upper  
65 arm BCF and observed that venous stenosis was common and that 40% of patients  
66 experienced thrombosis that resulted in loss of access. We and others found that AVF  
67 placement predisposed the cephalic vein to increased blood flow velocity, pulsatile flow,  
68 areas of low WSS, and increased risk of stenosis and thrombosis [8-13].

69         Past computational fluid models have shown the importance of the endothelium in  
70 thrombosis and established the flow and direction of WSS [10, 14] in the AVF, but these  
71 models do not provide a research platform with which to perform time-dependent  
72 perfusion experiments for testing hypothesis or intervention options. Given the larger  
73 cephalic vein diameters and increased flow rates associated with AVF, microfluidic  
74 systems used to study arterial circulation are not applicable to study complex patient-  
75 specific hemodynamics in large vein geometries [15]. This paper highlights the  
76 development of a novel application of routine diagnostic measures such as Intravascular  
77 Ultrasound (IVUS) and venogram to create patient-specific millifluidic models of the  
78 cephalic vein arch downstream of flow in the AVF. We detail the fabrication of transparent

79 elastomer-based millifluidic models *in vitro* that capture actual patient-specific  
80 dimensions, overall geometry and local topography of their venous cephalic arches as  
81 areas for clinical follow-up. We validate the fidelity of our design and fabrication workflow  
82 using IVUS and optical measurement on such an elastomeric device prototype. We then  
83 build six fluidic devices, including two idealized ‘physiologic’ and ‘pathologic’ models and  
84 four devices that recreate the cephalic arches of two hemodialysis patients at two time  
85 points from IVUS and venogram data. All six models are perfused with a transparent,  
86 engineered fluid matching the viscosity and density of blood and containing trace amounts  
87 of fluorescent microbeads under steady-state physiological conditions and imaged  
88 extensively to characterize flow in each device. Briefly, the tracer beads are imaged under  
89 epifluorescence and images of the microbeads under flow are acquired in time-series on  
90 each device’s cephalic arch or ‘bend’, along with areas upstream (prebend) and  
91 downstream (postbend) to the bend. We also developed image analysis software to  
92 extract the velocity and WSS of the fluorescent tracer beads from the imaged streamlines.

93 Although the current study details the geometry-hemodynamics interplay under  
94 physiologic flow parameters but is unable to implement pathologic flow rates or pulsatile  
95 waveforms, these models enable a comprehensive study of thrombosis under pathologic  
96 flow upon further optimization. The aspiration is that the geometry and hemodynamics in  
97 the fluidic model matching the patient-specific abnormal flow conditions will help tease  
98 out the variability in thrombosis risk and outcome between patients. Our technology  
99 shows promise for systematic isolation and analysis of vein geometry, flow parameters,  
100 blood constituents, and endothelial cell activation. All factors play a critical role in the  
101 nucleation and propagation of thrombosis in an AVF. Therefore, these factors are worth  
102 studying, both individually and collectively, to help develop personalized care in  
103 hemodialysis that improves the quality of life for ESRD patients.

104

## 105 **2. Materials and methods**

106

### 107 **2.1. Device fabrication**

108 Two time point-specific 3D models of the cephalic arches of two patients (P96 and  
109 P104) were reconstructed from IVUS and venogram of the cephalic arch taken 3 and 12  
110 months (mo.) after AVF placement [13]. The physiologic and pathologic models were  
111 created in AutoCAD with an average diameter of 3 mm (physiologic) and 6 mm  
112 (pathologic) and bend angle of 125°. Importantly, the physiologic cephalic arch is much  
113 smaller than the (enlarged) pathological and patient-specific geometries presented in this  
114 study [16]. Significant and continuous dilation of the cephalic vein in patients accompany  
115 cephalic arch remodeling after AVF placement which is necessary to withstand high flow  
116 rates and pulsatile flow transmitted through the AVF from the bypass artery. These  
117 abnormal flow patterns transmitted into the cephalic arch through the AVF can perturb  
118 the steady-state, low-velocity flow seen under physiological conditions. We doubled the  
119 cephalic arch diameter to capture this vein dilation in the pathologic model.

120 Each model (**Fig. 1A**) was imported into AutoCAD and two cones, each 2 cm in height,  
121 were added to the two ends of each model to help stabilize the flow at the junctions  
122 between the vein model and the flow system (**Fig. 1B**). Additionally, a box-like mold was  
123 designed to ease fabrication of the millifluidic devices. The vein and box mold were  
124 exported as a .stl file and imported to Cura LulzBot Edition 3.2.21 software. 3D printing  
125 parameters were set to 0.38 mm resolution, printing temperature of 210°C, with densities  
126 of 100% and 10% for the print and support, respectively. After adjusting the Print Setup,  
127 the file was exported as a GCode File (\*.gcode) and transferred to the Taz4 3D printer  
128 (#LUKTPR0041NA, B&H Photo) using a water-soluble, polyvinyl alcohol (PVA;  
129 #PVA300N05, eSUN), filament (**Fig. 1C**).

130 Once the device and box mold were printed, the box mold was glued to a 150 mm  
131 x 15 mm polystyrene Petri dish (Sigma) with a hot glue gun. Polydimethylsiloxane (PDMS;  
132 Catalog # 4019862, Dow Sylgard 184) was mixed at 1:10 (cross-linker: base) ratio and  
133 poured on the inside of the box mold to form an initial thin layer. Air bubbles trapped within  
134 the PDMS mix were removed by placing the Petri dish in a vacuum desiccator for 30 min  
135 before curing at 65°C for 2 hr. Subsequently, the 3D printed vein model was cleaned to  
136 remove all support filament and placed on top of the cured PDMS layer. Another PDMS  
137 layer was poured on the box and cured, covering half the height of the vein print. Upon  
138 vacuuming and curing, a final PDMS layer was poured and cured to completely cover the  
139 vein print. This resulted in a PDMS block with 3D printed vein embedded (**Fig. 1D**). The  
140 surrounding 3D printed box mold was removed by cutting out the PDMS block with a  
141 scalpel.

142 A 1 mm biopsy punch was used to cut into the PDMS to access the tips of the inlet  
143 and outlet cones. The device was immersed in DI water and autoclaved in a B4000-16  
144 BioClave Research Autoclave (Benchmark Scientific) 4-5 times at 134 °C, 30 psi until the  
145 PVA printed models within the solidified PDMS block were dissolved (**Fig. 1E**). Once  
146 dissolved, a cavity that recapitulates the patient-specific vein geometry (as reconstructed  
147 by us from IVUS and venogram data) remained inside the PDMS device. The millifluidic  
148 device was submerged in boiling water and wiped rapidly to remove any PVA particulate  
149 adsorbed onto the device surface. Unless removed, the PVA particulate coating makes  
150 PDMS surfaces significantly cloudy, which can deteriorate quality of fluorescent images  
151 of the device.

152 Since relatively high flow rates are necessary to mimic physiologic flow of the cephalic  
153 arch, it is critical that leakage-free connections between the fluid reservoirs and millifluidic  
154 devices are established. Given that our fluid reservoirs have tubing ports compatible with  
155 1/16" outer diameter (OD), 1/32" inner diameter (ID) PEEK tubing and our millifluidic  
156 devices have inlet/outlet ports compatible with 1/16" ID, 1/8" OD Tygon PVC clear tubing  
157 (#6516T11, McMaster Carr), a cuffed tube-tube connection adapter was made to couple  
158 tubing. To achieve this, the ring portion of 8-gauge AWG crimp ring terminal connectors  
159 (#IGCRT8-10, Amazon) were cut with a sheet metal cutter (#DWHT14675, Amazon) in  
160 order to obtain a cast-able cylindrical mold. Around 4 cm of the PEEK tubing was inserted

161 into the Tygon tubing. A rubber sleeve was positioned to tightly cover the PEEK tubing-  
162 Tygon tubing connection placed in the center of the mold. The bottom of the cylindrical  
163 mold was then sealed with Parafilm M wrapping film (#S37440, Fisher) to keep tubing  
164 components in place. The PEEK tubing-Tygon tubing junction was positioned vertically  
165 such that both tubing ends were coaxially aligned relative to the cylindrical mold. Low-  
166 viscosity epoxy resin (#4336899262, Amazon) was poured into the cylindrical mold to  
167 encase the tubing junction. The resin was allowed to cure at room temperature for at least  
168 24 hr. to ensure that any potential leaks in the tubing junction were sealed (**Fig. S1A**).

169 To stabilize the junction between the millifluidic device and the coupled tubing  
170 adapter, two small 3D-printed box molds were used to cast PDMS (**Fig. S1B**). Plastic  
171 barbed tube fittings (3/32" OD x 1/16" ID, #5117K41, McMaster-Carr) were plugged into  
172 both the inlet and outlet of all devices (**Fig. 1F**). The smaller box molds were aligned with  
173 the device inlet and outlet and affixed to the device using a hot glue gun. The Tygon-  
174 tubing end of the tubing adapter was connected to the barbed fitting at the device inlet  
175 through a hole in the small box mold; the outlet tubing was similarly attached to the barbed  
176 fitting on the device outlet. Finally, PDMS (1:10 crosslink/elastomer) was cast and cured  
177 on the small box molds to seal the junctions. The inlet tubing was connected to the fluid  
178 reservoir; the pressure-driven flow control system was also connected to the fluid  
179 reservoir to drive unidirectional flow in the millifluidic devices (**Fig. 1G**). The outlet tubing  
180 was allowed to drain out at atmospheric pressure. Six fluidic devices were fabricated:  
181 physiologic, pathologic, patient P96 imaged 3 (P96, 3 mo.) and 12 months (P96, 12 mo.)  
182 after AVF placement, and patient P104 also imaged 3 (P104, 3 mo.) and 12 months  
183 (P104, 12 mo.) after AVF placement. All fabricated devices are displayed in **Fig. 1H-M**,  
184 along with their average vein 'lumen' diameters.

185 Additionally, 'phantom' device, based on a patient (P98, 3 mo., average vein  
186 diameter = 8.5 mm) chosen at random, was created for geometric validation of our device  
187 fabrication method (**Fig. 2A**), to check if the internal cavity geometry of fabricated  
188 'phantom' matched the geometry of the computational model it was based on. The  
189 inlet/outlet ports were simplified in the phantom model since flow was not necessary to  
190 image the internal cavity of this device.

## 191 **2.2. Validating device fidelity in recapitulating cephalic arch geometry**

192 To confirm that the internal vein geometry of our millifluidic devices match the  
193 geometry of the computational models they are based on, we performed IVUS on the  
194 millifluidic phantom device, henceforth referred to as the 'phantom'. We generated 3D  
195 computational models constructed from each IVUS pullback imaging performed on the  
196 phantom device that could be used for geometric comparison. This process was followed  
197 to test consistency of IVUS imaging across different trials, as well as for fidelity of our 3D  
198 modeling and device fabrication processes in recapitulating vein geometry. We reasoned  
199 that if our phantom millifluidic model was faithful to the IVUS images, then the models  
200 reconstructed from different rounds of IVUS imaging of said device would match each  
201 other, as well as the original model used to fabricate the millifluidic device in the first place.

202 The millifluidic phantom device (**Fig. 2A**) was filled with 1x phosphate buffered saline  
203 (PBS), punctured using a 21G micro-puncture needle and a 0.018" micro-puncture wire  
204 was inserted into the 'lumen' of the model, which served as a guide wire for the imaging  
205 catheter (**Fig. 2B**). Next, a 4 French (Fr) micro-puncture sheath was advanced over the  
206 guidewire and exchanged via a 0.035" guidewire for a 5-Fr Cordis vascular introducer  
207 sheath (Cordis Corporation, Miami Lakes, FL), de-gassed, flushed and secured in place.  
208 Then, a Hi-Torque Floppy II coronary guidewire (Abbott Vascular, Santa Clara, CA) with  
209 0.014" x 190 cm dimensions was introduced into the lumen of the phantom and positioned  
210 distally. Finally, a Philips Volcano Eagle Eye Platinum 20 MHz Intravascular Ultrasound  
211 (IVUS) catheter was prepared, flushed and introduced over the coronary guidewire into  
212 the millifluidic phantom model and subsequently positioned within the proximal cephalic  
213 arch to simulate the *in vivo* starting IVUS position. The IVUS catheter was calibrated using  
214 the portable IVUS imaging console (**Fig. 2C**) to eliminate near-field ring-down artifact and  
215 the field of view was adjusted to ensure full circumferential visualization of the model (**Fig.**  
216 **2D**). Interestingly, the contrast of the lumen images was higher in the PDMS millifluidic  
217 phantom model than in actual patient cephalic veins. Two independent IVUS pullback  
218 recordings in grayscale were performed using a research-quality pullback sled at a rate  
219 of 1.0 mm/s.

220 Venogram imaging was not required on the PDMS device; PDMS being transparent,  
221 allowed direct imaging of the general contour of the vein when perfused with food color  
222 dye. This image was processed using 'threshold' and 'skeletonize' functions in NIH  
223 ImageJ [17] to obtain the vein path. This was combined with the IVUS images of the  
224 millifluidic phantom device obtained as described above to reconstruct 3D models [13].

### 225 **2.3. Flow setup**

226 Millifluidic devices were imaged on an Olympus IX83 microscope (**Fig. S2C**), perfused  
227 with blood-mimicking fluid (BMF, distilled water with 6.3 % (w/v) Dextran, D4876-50G,  
228 Sigma-Aldrich) to match the viscosity and density of whole venous blood and containing  
229 trace amounts ( $4 \times 10^{-6}$  %, v/v) of 2- $\mu$ m fluorescent polystyrene microbeads (Catalog #  
230 FCDG008, Bangs Labs). A concentration of 4 % Dextran in BMF (w/v) with a viscosity of  
231 2.4 mPa.s was also used in some flow experiments. BMF was perfused into the millifluidic  
232 devices under physiologic steady-state flow at 20 mL/min [18], using an OB1 MK3+  
233 pressure-driven flow control system (Elvesys, France; **Fig. S2C**). Component diagram of  
234 the fluidic circuit is shown (**Fig. 2E**).

### 235 **2.4. Imaging**

236 The steady-state flow at 20 mL/min, represents a healthy flow rate for non-arterialized  
237 cephalic veins [18]. BMF was flowed at 20 mL/min into each device at steady-state to  
238 characterize WSS in the device as a function of local vein geometry; the flow rate was  
239 maintained while the cephalic arch models were imaged close to the device wall using  
240 epifluorescence microscopy. Image quality limitations only allowed imaging in areas close  
241 to the PDMS-BMF interface of the millifluidic device, henceforth referred to as the 'vein

242 wall'. Focusing deeper into the BMF resulted in higher background fluorescence and also  
243 made the vein wall substantially more difficult to resolve in the images.

244 We imaged tracer beads flow close to the wall ( $\leq 400 \mu\text{m}$ ) which was sufficient to  
245 calculate WSS across all ROI in all models. Flow streamlines adjacent to the vein wall  
246 should accurately capture local flow velocities and WSS. Videos of flow trajectories of the  
247 fluorescent beads were imaged under 6.4X magnification (using a 4X, NA=0.16 objective  
248 and 1.6X built-in microscope magnification) at 40 frames per second (fps) and 50-100 ms  
249 exposure times (depending on device), using a Hamamatsu ORCA Flash4.0 camera and  
250 MetaMorph software (Molecular Devices, USA) under GFP illumination (488 nm/510 nm).  
251 Videos consisting of 100 image frames, each frame containing 2048x2048 pixels, of  
252 tracer-bead streamlines were obtained from 18-22 positions, each referred to as a Region  
253 Of Interest (ROI), per device. At least 10 streamlines were extracted per image frame.  
254 This yielded fluorescent streaks of reasonable lengths from which local flow velocities  
255 were calculated across outer and inner walls of prebend, bend and postbend regions (**Fig.**  
256 **2F**). Note that for a given flow velocity, longer exposure times lead to longer fluorescent  
257 streaks in the images (**Fig. S1D-F**). Videos of 100 image frames each were acquired per  
258 ROI and saved as 16-bit .tiff files for subsequent data processing off-line. Overall, 18-22  
259 ROIs were captured at a given flow rate per device, across prebend, bend and postbend  
260 regions.

## 261 **2.5 Image processing**

262 All videos needed to be pre-processed with a macro-code written in NIH ImageJ [17]  
263 to extract a) high-contrast streamlines, and b) outline of the vein wall for any given ROI,  
264 before using our automated Python-based pipeline to calculate flow velocity and WSS.  
265 ImageJ pre-processing (**Fig. S2A**) consisted of the following functions performed  
266 sequentially on each raw image stack (**Fig. 3A**): contrast enhancement, background  
267 fluorescence subtraction, de-speckling, brightness and contrast adjustment (**Fig. 3B**),  
268 threshold adjustment (**Fig. 3C**), binarization, and 'Analyze Particles' to filter streamlines  
269 by size and circularity (**Fig. 3D**). The 'Analyze Particles' function is also useful to filter out  
270 image artifacts like diffraction rings, small debris, etc. Streamlines out of the focal plane  
271 that are less bright than the streamlines in the focal plane were filtered out. Given that  
272 experimental conditions such as flow rate, exposure time, magnification and numerical  
273 aperture of the objective, bead concentrations, etc. affected streamline quality and varied  
274 between experiments, the function parameters in the macro-code needed to be adjusted  
275 for each tiff-stack.

276 Identifying the vein wall boundary in the ROIs is important to calculate WSS. A  
277 maximum intensity Z-stack projection was made on the tiff-stack to generate a single wall  
278 boundary image from each ROI (**Fig. 3E**), manually outlined, binarized (**Fig. 3F**) and  
279 added to each frame of processed streamlines, using the '*Image Calculator*' function.  
280 These image pre-processing steps generated .tiff files of 100 frames each for each ROI,

281 with each frame containing binarized streamlines of fluorescent beads and the vein wall  
282 outline (**Fig. 3G**).

283 Since the binarized images produced by the ImageJ preprocessing were less  
284 susceptible to variation, we developed a customized image processing pipeline in Python  
285 to calculate velocity and WSS from the pre-processed data from each ROI. Individual  
286 image frames ordered in time were generated in .tiff format for analysis. To extract velocity  
287 streamlines in each image frame, we used the '*connected components detection*'  
288 algorithm [19] in OpenCV, an open-source software package for computer vision [20], to  
289 obtain all connected objects in each image frame. Next, we assigned a tight bounding  
290 box to each connected component. Bounding boxes of those connected components that  
291 met the following criteria were selected as velocity streamlines per frame: size in pixels  
292 (area of the fitted bounding box ranging between [75, 9000]), shape (height/width ratio of  
293 the bounding box between [3, 100]), height between [15, 500], and width < 50.

294 After assigning velocity streamlines to each frame, we aggregated all streamlines in  
295 an ROI (as time series .tiff) into a global frame. We reconstructed the vein wall boundary  
296 per frame from the binarized contour of the wall boundary marked in each frame. We  
297 projected the velocity streamlines perpendicularly onto the wall boundary. For each pixel  
298 in the wall boundary, we searched all streamlines in the frame and collected those  
299 streamlines that were projected at 90° onto the pixel point on the wall boundary (**Fig. 3H**).  
300 We also used the measured viscosity of the BMF and the perpendicular distance of  
301 detected streamlines to the wall boundary to calculate WSS. If multiple streamlines were  
302 projected to the same pixel in the wall boundary, an average WSS value was computed  
303 for the pixel.

304 Using the pipeline described above, we calculated frame-by-frame information on  
305 streamline count, mean velocity (mm/s) and mean WSS (mPa). Violin plots of the mean  
306 and distribution of velocity (red) and WSS (green) calculated from the streamlines in each  
307 frame are shown for a series of 100 frames acquired consecutively over time (**Fig. 3I**) for  
308 an ROI chosen at random from the outer (top) and inner (bottom) walls of the prebend,  
309 bend and postbend regions of the pathologic model. For any given ROI, the velocity and  
310 WSS values fluctuate around an average that remains stable over time, as expected for  
311 constant flow rate.

## 312 **2.6. Theory and calculations**

313 Wall shear stress,  $\tau$  was calculated as:

$$314 \quad \tau = \eta \frac{v}{h},$$

315 where  $\eta$  is the fluid's dynamic viscosity,  $v$  is the streamline velocity and  $h$  is the distance  
316 between streamline and vein wall boundary.

317 Though the viscosity,  $\eta$  of blood and BMF are shear-thinning [21], we use an average  
318 value (3.5 mPa·s) for simplicity. This value was measured in BMF, using a rotational

319 rheometer (Anton Paar MCR 301) under physiologic shear rates (20-200 s<sup>-1</sup>) [22] The  
320 coefficient of variation (CV) for WSS is calculated as  $CV(\%) = \left( \frac{\text{standard deviation}_{WSS}}{\text{mean}_{WSS}} \right) * 100$ . Given that a fixed flow rate was used in all experiments and vein diameter and  
321 surface topography influence flow velocity and WSS, we use CV to characterize and  
322 compare flow properties in geometrically diverse cephalic arch models used in this study.  
323

324

### 325 3. Results

#### 326 3.1. Validating phantom model

327 Two series of IVUS pullback measurements were performed on the phantom,  
328 referred to as 'OG', (**Fig. 4A**), each of which was used to generate a 3D model *in silico*  
329 (**Fig. 4B, C**), referred as 'Val1' and 'Val2', respectively. 2D images of Val1 and Val2 in the  
330 xy-plane were captured at 5° rotational increment along the z-axis and co-axial to prebend  
331 vein path, up to 180° to compare the 3D models. Snapshots of OG, Val1 and Val2 were  
332 overlaid at each rotational angle and the overlap areas were calculated to quantify the  
333 differences in local topography. **Fig. 4D** shows the models (in black) at rotational angles  
334 of 0°, 45° and 90°, along with their area overlap (white).

335 The total area projection in xy-plane for OG, Val1 and Val2 across 180° rotational  
336 angles are shown in **Fig. 4E**, with an average overlap of  $95.05 \pm 3.92\%$  (**Fig. 4F**). This  
337 suggests that our 3D modeling of patient veins using IVUS and venogram imaging and  
338 3D printing fabrication method yield reproducible vein models with relatively accurate  
339 representations of vein topographies. The Pearson correlation of the total areas between  
340 OG, Val1 and Val2 are > 0.5 across all rotational angles (**Table 1**). The area correlation  
341 between Val1 and Val2 is higher ( $r_{(Val1\_Val2)} = 0.99$ ) than either of these models with  
342 respect to OG ( $r_{(OG\_Val1)} = 0.66$  and  $r_{(OG\_Val2)} = 0.62$ ). We noted that IVUS imaging of the  
343 lumen in PDMS device offered higher contrast (**Fig. 2D**) compared to IVUS images of  
344 veins, potentially due to difference in material properties, leading to higher r value. Lower  
345 area correlation between the original and validation models could also result from the  
346 limited 3D-printing resolution. Overall, we see good agreement between the original and  
347 reconstructed models.

#### 348 3.2. Hemodynamics under steady-state physiologic flow

349 ROIs in each device were grouped by the inner and outer walls of the prebend,  
350 bend and postbend regions and their WSS values were averaged to obtain a  
351 representative value for these regions. Average WSS values in the inner prebend, inner  
352 bend, inner postbend, outer prebend, outer bend and outer postbend regions in each  
353 device are shown in **Fig. 5A**. When averaging across all ROIs in a given model, we found  
354 that the highest average WSS value of  $255 (\pm 54)$  mPa was measured in the 'physiologic'  
355 device with the smallest average vein diameter (**Table 2**). Conversely, the lowest average  
356 WSS value ( $27 \pm 6$  mPa) was measured in the 'P104, 12 mo.' device that also had the  
357 largest average vein diameter (**Table 2**). Overall, average WSS, calculated for all ROIs

358 in a device, scaled inversely with the average vein diameter of the device, as expected  
359 (**Fig. S3D**).

360 WSS values measured in the physiologic model under physiological flow rates  
361 ranged between  $203 \pm 73$  mPa in the inner bend to  $346 \pm 229$  mPa in the outer prebend  
362 regions (**Fig. 5A**). Note that these values lie within the range of physiologic WSS values  
363 reported earlier [23].

364 Next, we compared WSS in the physiologic and pathologic models that have same  
365 arch angle but different vein diameters (3 and 6 mm, respectively). We measured  
366 relatively symmetric WSS in the bend region and striking asymmetry in the postbend  
367 region in the physiologic model (**Fig. 5A, S3A**). This agrees with fluid dynamics principles  
368 in pipe flow at geometric bends [13], where higher velocities are expected at the outer  
369 wall of the postbend region, along with lower velocities close to the opposite wall (inner  
370 bend). WSS polarization in the prebend region is absent in the pathologic model,  
371 consistent with shorter velocity streamlines measured in the pathologic model, at similar  
372 volumetric flow rates [13].

373 Focusing on the patient models, despite patient P96 having similar average  
374 diameters (6.6 mm) and arch angles ( $133^\circ$  and  $132^\circ$  at 3- and 12-mo., respectively), we  
375 identified significant geometric remodeling of the cephalic arch in 3D, particularly at the  
376 postbend region, which narrowed between 3 and 12 mo. (**Fig. S3A**). These geometric  
377 changes influence resulting WSS across different regions of the cephalic arch. For  
378 example, we observed increase in WSS in the prebend region and the outer wall of the  
379 postbend region from 3 to 12 mo. Moreover, WSS evens out in the bend region at 12-  
380 months, which contrasts the striking asymmetry observed at 3 mo. These findings indicate  
381 that vein dilation and remodeling can prominently affect hemodynamics in the cephalic  
382 arch through geometric and topographical changes.

383 Using the pathologic and P96 models to compare veins of similar sizes (6 and 6.6  
384 mm, respectively), we note differences in WSS patterns in the prebend and bend regions  
385 between the models. Except for the postbend region, the pathologic model has similar  
386 WSS magnitudes on the inner and outer walls. This is not the case for P96 models at 3  
387 and 12 mo. where WSS is asymmetric in the inner and outer bend, across all regions.  
388 This is most likely due to the uneven topography of the vein walls in P96, compared to  
389 the smooth wall of pathologic model and symmetric geometry along the vein lumen (**Fig.**  
390 **5A, S3A-B**). For patient P104, the average vein diameter increases from 9 mm to 11 mm  
391 and arch angle decreases from  $125^\circ$  to  $115^\circ$  between 3 and 12 mo., respectively (**Fig.**  
392 **5A, S3C**). Except for the outer bend region in P104, there is consistent decrease in WSS  
393 at decreased flow velocity due to increase in vein diameter (at fixed volumetric flow rate).

394 Since we are also interested in gauging variability in patient outcome, we quantified  
395 the WSS CV across the geometrically distinct models in context of vein diameter and  
396 topography. At fixed volumetric flow rate, we measure greater CV in average WSS with  
397 increased vein diameter (**Fig. 5B**). Devices with narrower veins, e.g., physiologic device

398 (3 mm), show lower average WSS CV (74%), whereas devices with larger vein diameter  
399 (11 mm in P104, 12 mo.) record larger CV (162%, **Table 2**). We also characterized WSS  
400 and CV in the pathologic and P104 (3 and 12 mo.) devices at 20 mL/min at two different  
401 viscosities, 2.4 and 3.5 mPa·s (**Fig. S3E, 5C**), by adjusting the concentration of dextran  
402 in BMF (4 and 6.3 %, w/v, respectively). We found reproducible trends at these viscosities,  
403 where WSS CV increased systematically with average vein diameter: the pathologic  
404 model (6 mm) showed the lowest CV, followed by the CV in P104, 3 mo. (9 mm) and  
405 P104, 12 mo. (11 mm) models (**Fig. 5C**). We noted lower average WSS and standard  
406 deviation at 2.4 mPa·s, compared to 3.5 mPa·s (**Fig. S5E**). These results highlight the  
407 complexity of the system where vein diameter, geometry, surface topography and  
408 viscosity contribute to WSS in the cephalic arch.

#### 409 **4. Discussion**

410 In the current study, we present the design and operation of a novel patient-specific  
411 model of the venous cephalic arch to accurately measure WSS. We validated the fidelity  
412 in recreating patient vein geometry in the model, using IVUS imaging and infused these  
413 models with engineered fluids that mimic blood density and viscosity under physiologic  
414 flow conditions on the devices. We imaged the details of the particles flowing through our  
415 model vessel and constructed a semi-automated image analysis pipeline to determine  
416 WSS. WSS is an important measurement as the magnitude of the WSS in a cephalic vein  
417 is a predictor of vein remodeling in AVF. Currently, it is not possible to measure WSS  
418 accurately in clinical practice and past computational models defining WSS are limited in  
419 imaging and validation [24]. The clinical relevance of this tool, however, is yet to be  
420 determined.

421 This study presents the fabrication of fluidic models that recreate patient-specific vein  
422 geometry using radiologic and ultrasound imaging. We saw that average WSS decreased  
423 with increase in average vein diameter (**Fig. S3D**); however, patient-specific vein  
424 geometry and wall topography also influenced WSS. CV in average WSS, however,  
425 roughly increased with increase in vein diameter (**Fig. 5B**). Surface topography does not  
426 seem to be a major contributor to WSS CV under physiologic flow condition. For example,  
427 comparing the pathologic and P96 models with roughly similar vein diameters but marked  
428 different geometry and wall topography, the pathologic model recorded lower WSS than  
429 the P96 models but all three models showed similar CV.

430 Blood viscosity, a crucial factor influencing WSS, can fluctuate over time in a patient-  
431 specific manner [25]. We identified significant effect of viscosity on WSS (**Fig. S3E**) but  
432 not on its CV (**Fig. 5C**). Changes in whole blood viscosity and WSS likely trigger  
433 endothelial cell activation before and after hemodialysis sessions where solute  
434 concentrations and osmotic pressures are readjusted, especially when treatment is  
435 administered three times a week [26].

436 *Limitations and future directions:* An eddy in the prebend region (**Fig. S4A**), generated by  
437 a mismatch in tubing and device diameters, prevented us from imaging steady-state

438 laminar flow throughout the device. In future studies, we will mitigate the effect by  
439 replacing our current connection tubing of 1/32" ID with wider tubing. This will create a  
440 more gradual transition in flow velocities from tubing to vein model, thus decreasing the  
441 size of the eddy. Preliminary experiments with wider tubing seem to eliminate any eddy  
442 formation in the prebend region (**Fig. S4B**), though further experiments are needed to  
443 confirm if this holds true across all models and different experimental conditions. We also  
444 expect that larger ID connection tubing will allow us to achieve (higher) pathologic flow  
445 rates. Note that the size and magnitude of this eddy in the prebend also depend on  
446 viscosity, a parameter that varies from patient to patient.

447 Currently, our models reliably achieve flow rates of 20 mL/min seen in physiologic  
448 conditions but falls far short of flow rates > 600 mL/min seen in patients under  
449 hemodialysis [15]. Additionally, we are developing the capability to modulate flow rates in  
450 a programmable way on our current setup to match patient-specific pulse profiles, along  
451 with data processing tools to calculate WSS under pulsatile flow [12]. These flow  
452 parameters are also of interest since pulsed flow in veins, coupled with dramatically  
453 increased flow rates might synergize together, resulting in thrombosis and clotting  
454 pathology in the hemodialysis population.

455 Due to limitations in imaging setup (objective with low NA (0.16), imaging through thick  
456 layers of PDMS and high scattering), we were unable to image deep into the fluidic  
457 devices. As a consequence, we limit WSS measurements to the lower half of the vein  
458 (closer to the objective). However, the asymmetric geometry of the fluidic models requires  
459 better coverage in imaging the devices in the current configuration, including their upper  
460 half. This and overall better resolution in z axis can be achieved by using confocal  
461 microscopy, objective with high NA and long working distance, and lower concentration  
462 of tracer beads in flow experiments. Additionally, newer 3D printer models are now  
463 capable of XY and Z-layer printing resolutions that surpass TAZ4 3D printer used in this  
464 study. It is reasonable to expect higher correlations and area overlap between original  
465 phantom and validation models by using 3D printers with higher spatial resolution.

466 Finally, adding a layer of endothelial cells to the inner walls of these millifluidic devices  
467 [27] and quantifying their biochemical responses under flow [28-30] are necessary to  
468 biologically complement generated WSS profiles [13].

469 Nonetheless, the present work shows that we have developed a robust workflow and  
470 image analysis pipeline to characterize WSS under healthy, physiologic flow conditions,  
471 a base knowledge needed to contrast from pathologic findings in the future. Also, if  
472 venous blood clots can be recreated *in vitro* in our devices, extracted and studied by  
473 histological and biochemical methods, they can lead to the synthesis of novel and more  
474 efficient anticoagulant and thrombolytic therapies that help decrease lethal thrombotic  
475 events.

476

## 477 **5. Conclusions**

478 In this work, we explored diverse geometries of the cephalic arch in hemodialysis  
479 patients with AVF. Nonetheless, we must recognize that vein physiology is constantly  
480 evolving and adapting to genetic and environmental inputs, especially in artificial  
481 circulatory scenarios such as AVFs. Therefore, in order to address current AVF failure  
482 rate, we set out to design and fabricate patient-specific cephalic arch replicas in the form  
483 of millifluidic devices to characterize hemodynamics and WSS under physiologic flow. We  
484 also created an image analysis pipeline to characterize flow and calculate WSS from  
485 videos of tracer particle streamlines. We applied novel 3D printing and advanced  
486 biomedical imaging technologies to study fistulas and connected vessels that are affected  
487 by thrombosis. To our knowledge, this is the first experimental work to generate patient-  
488 specific AVF vein models to help characterize geometric and flow abnormalities that  
489 underlie thrombosis and associated pathologies in the clinical setting.

490

491

492 **Acknowledgements:** We thank all patients who gave their time for imaging procedures.  
493 This work made use of the shared facilities at the University of Chicago Materials  
494 Research Science and Engineering Center, supported by National Science Foundation  
495 under award number DMR-2011854.

496

497 **Funding:** This work was supported by the Ginny and Simon Aronson Research Award,  
498 University of Chicago Institute of Translational Medicine Pilot Award, and A.B.'s research  
499 development funds. A. M-R was supported by the NSF GRFP fellowship.

500

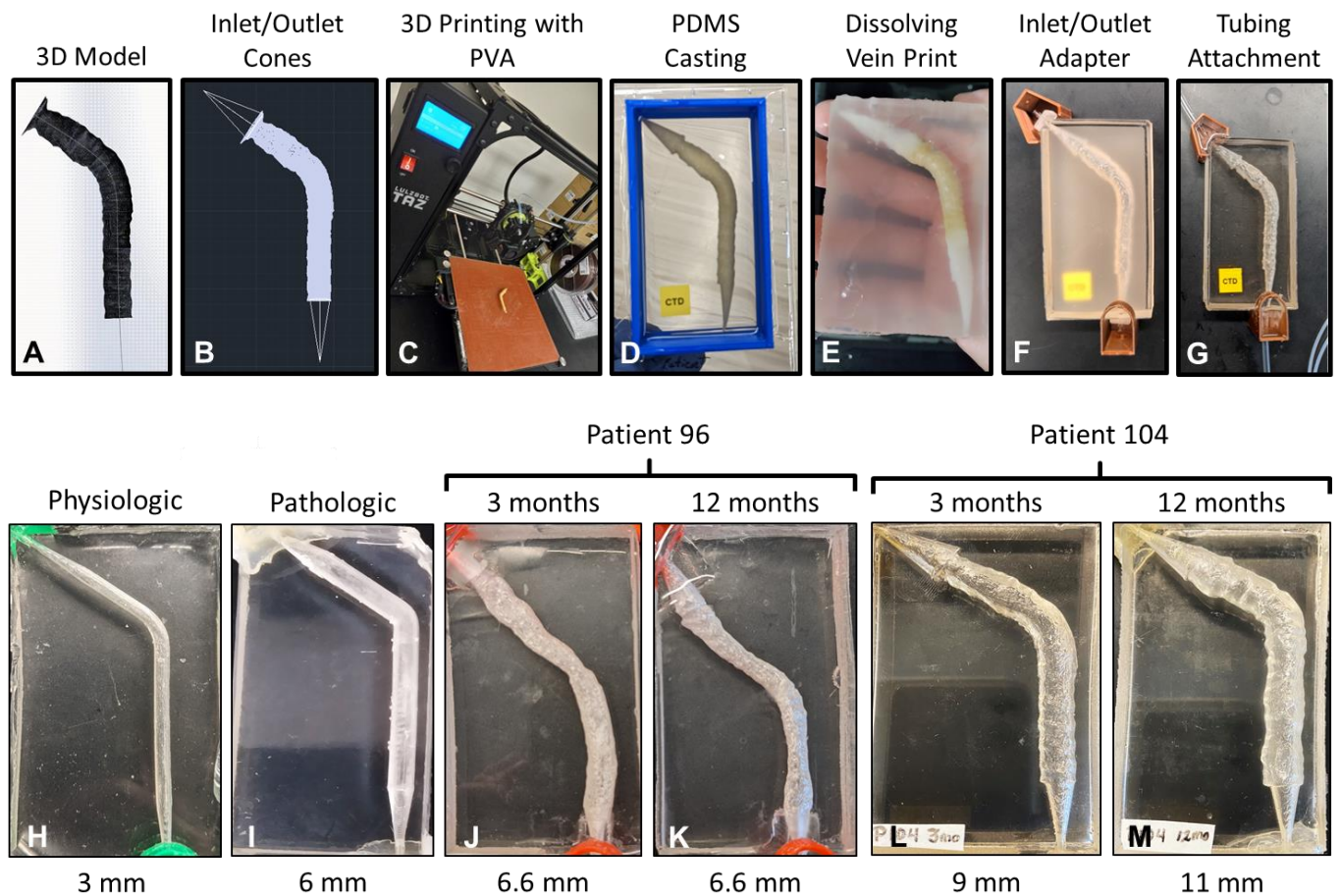
501

502 **Conflict of Interest:** All authors declare no competing interests.

503

504 **Figures**

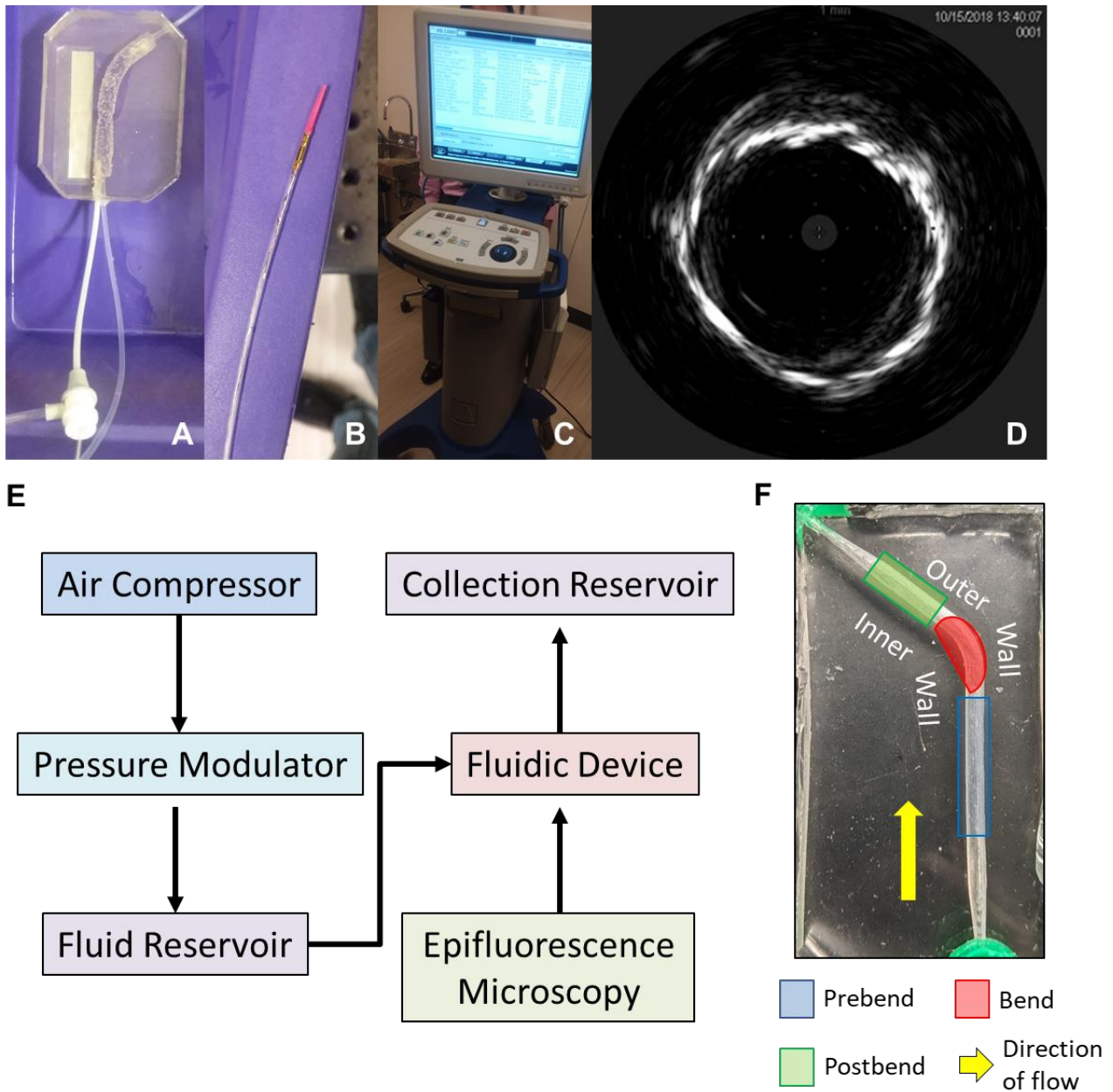
505



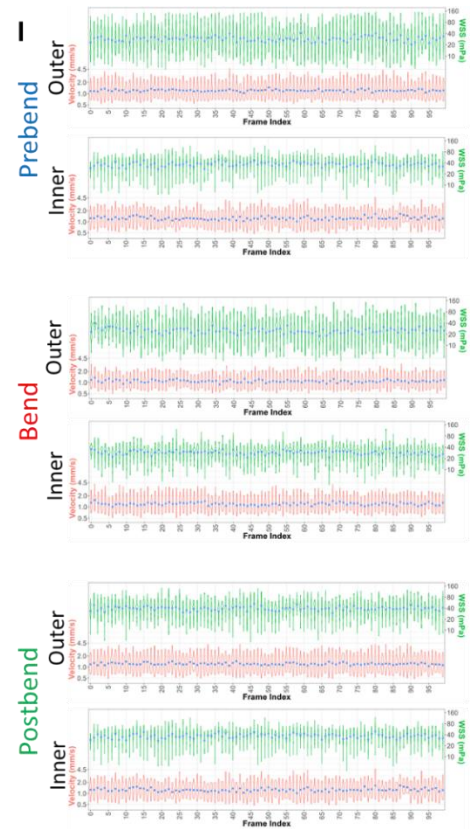
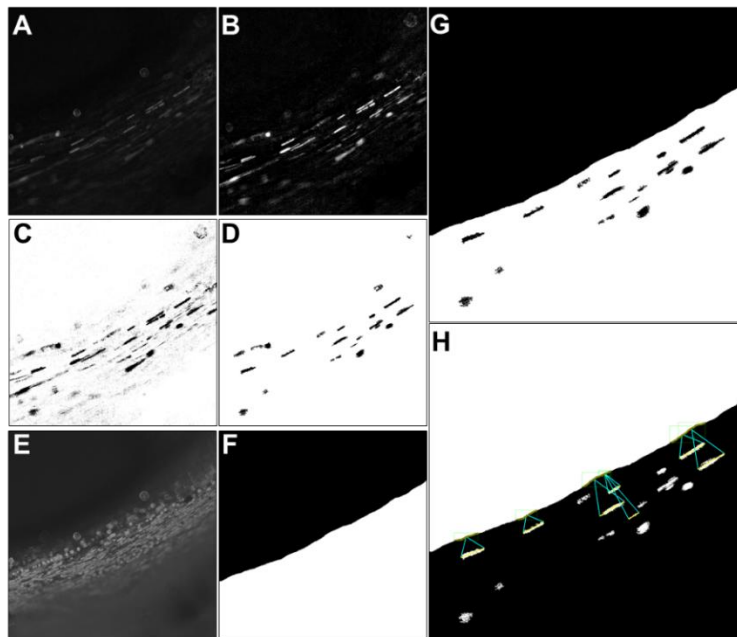
506 **Figure 1: Fabrication of cephalic arch millifluidic devices.** (A) Patient computational  
 507 cephalic arch model. (B) Inlet/outlet cones addition to computational model to make flow  
 508 setup tubing compatible with fabricated millifluidic device inlet/outlet dimensions. (C)  
 509 Computational model 3D printing with water-soluble PVA filament by material extrusion  
 510 3D printer. (D) Post-PDMS casting, the cephalic arch 3D print is encased in a PDMS  
 511 block. (E) Inlet/outlet holes are made in the PDMS blocks and these are submerged in  
 512 water and autoclaved to dissolve until 3D print is completely dissolved. (F) Inlet/outlet  
 513 adapters are incorporated to connect the millifluidic device to the flow setup and circuit.  
 514 (G) Tubing is attach to connect it to fluid reservoirs in order to perform flow experiments  
 515 and record them via epifluorescence microscopy. (H-M) Fabricated cephalic arch  
 516 millifluidic devices and respective average vein diameters (mm) capturing physiologic (H),  
 517 pathologic (I) and patient-specific geometries at 3 and 12 months post-AVF creation (J-  
 518 M).

519

520

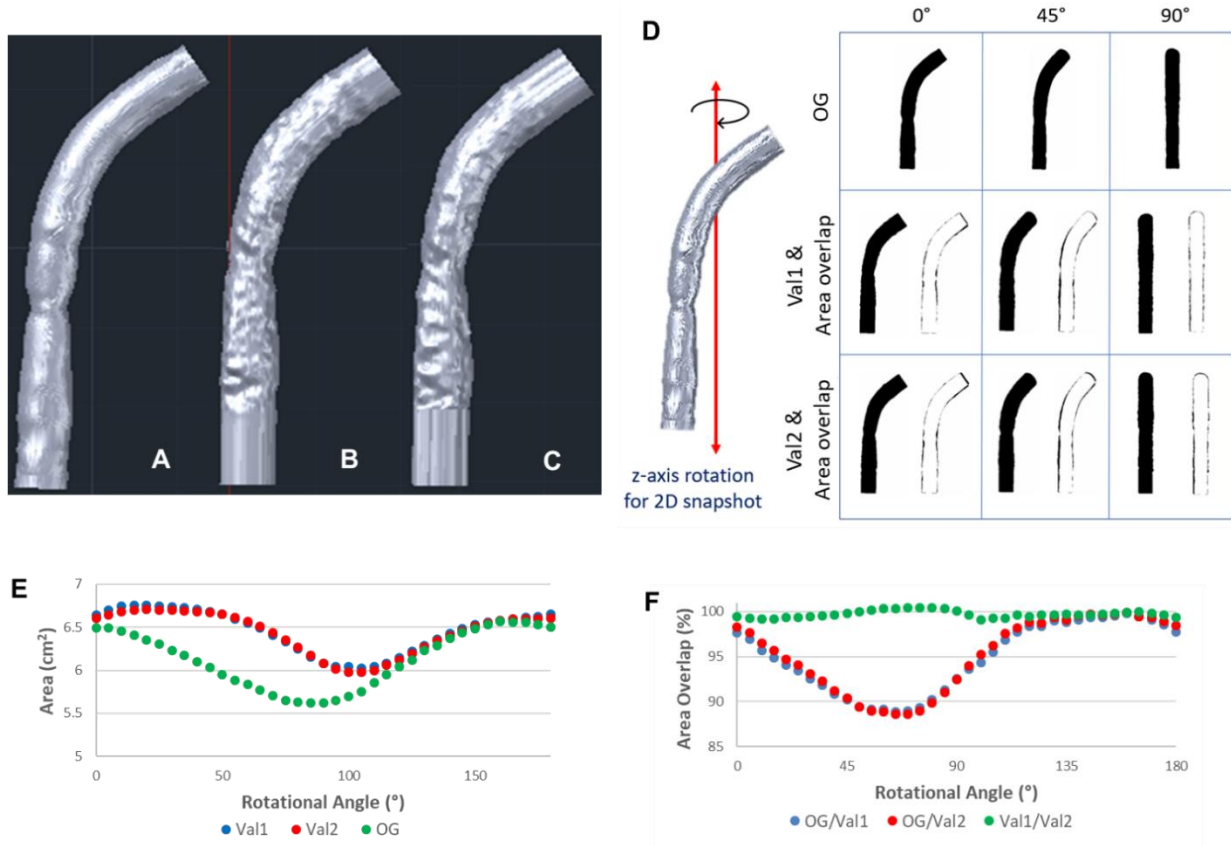


522 **Figure 2: Post-fabrication device geometric validation and flow imaging strategy.**  
 523 (A) Phantom model of the cephalic arch canulated with IVUS transducer catheter. (B)  
 524 IVUS catheter. (C) Portable IVUS imaging console. (D) IVUS image obtained from the  
 525 phantom model flushed with 1X PBS. (E) Component diagram of experimental  
 526 flow/imaging setup. (F) Vein region diagram showing prebend (blue), bend (red) and  
 527 postbend (green) and employed direction of flow (yellow arrow).



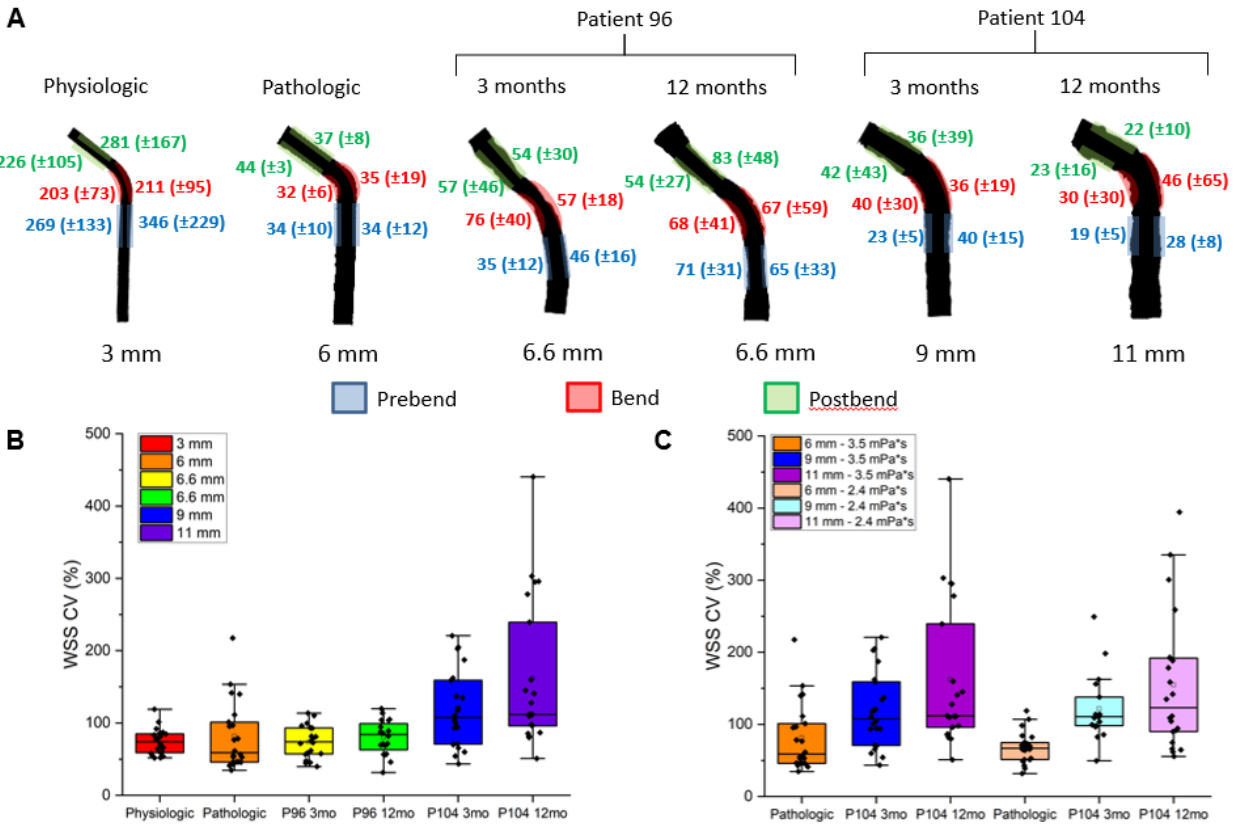
528

529 **Figure 3: Calculating streamline velocity and wall shear stress from particle**  
 530 **imaging velocimetry.** (A) ROI raw imaging data example from captured flow videos  
 531 across the cephalic arch millifluidic devices. (B) Highlighted streamlines after sequentially:  
 532 enhancing contrast, subtracting background, subtracting average intensity, despeckling  
 533 and adjusting brightness and contrast (the latter being ROI dependent). (C) ROI  
 534 dependent thresholding resulting in binary images that capture bright and well-defined  
 535 streamlines. (D) Particle filtering by means of Analyze Particle function and adjusting size  
 536 and circularity parameters to select for streamlines while filtering out low-quality out-of-  
 537 focus streamlines and diffraction artifacts. (E) Max intensity projection of flow videos that  
 538 facilitates outlining vein wall boundary. (F) Binary image generated after outlining vein  
 539 wall boundary. (G) Addition of vein wall outline to filtered streamlines (D+F). (H)  
 540 Streamline perpendicular projection onto vein wall boundary which allows calculating  
 541 WSS. (I) Flow video analysis output for six representative ROIs from the pathologic model  
 542 across the three main regions (prebend, bend and postbend) and wall sides (inner and  
 543 outer): WSS and streamline velocity violin plot across flow video frames.



544

545 **Figure 4: Validation of the computationally reconstructed phantom model.** (A)  
 546 Original phantom computational model used for device fabrication. (B-C) Validation  
 547 models reconstructed from IVUS and optical imaging performed on phantom millifluidic  
 548 device (replicates). (D) Geometric validation strategy schematic: all models were rotated  
 549 with respect to the z-axis and 2D images from top perspective were overlapped to  
 550 evaluate area overlap from 0-180° rotational angles with 5° rotational increments. (E)  
 551 Area values for all models across 180° of z-axis rotation. (F) Area overlap between  
 552 phantom computational models upon z-axis rotation.



553

554 **Figure 5: WSS profiles across cephalic arch millifluidic models.** (A) Experimental  
 555 WSS profiles depicts the average WSS (mPa) value per vein region and wall side under  
 556 normal physiologic flow of 20 mL/min using a blood-mimicking fluid. Vein model average  
 557 vein diameter (mm) is shown below each cephalic arch outline. (B) WSS CV box plot  
 558 across all models and their respective ROIs, average vein diameters shown on legend.  
 559 Flow data was collected using BMF with viscosity of 3.5 mPa\*s under physiologic flow.  
 560 (C) WSS CV box plot for pathologic and P104 cephalic arch models under physiologic  
 561 flow using BMF of varying viscosity (2.4 and 3.5 mPa\*s). Average vein diameters and  
 562 BMF viscosity are shown on legend.

Phantom Model	Mean Total Area (cm <sup>2</sup> )	Compared Models	Mean Area Overlap (%)	Area Pearson Coefficient (r)
Original	6.13 (±0.33)	$\frac{OG}{Val1}$	94.90 (±3.87)	0.66
Validation #1	6.46 (±0.25)	$\frac{OG}{Val2}$	95.20 (±4.08)	0.62
Validation #2	6.44 (±0.24)	$\frac{Val1}{Val2}$	99.70 (±0.40)	0.99

563

564 **Table 1:** Area comparative analysis of original and validation phantom computational  
565 models.

Model	Diameter (mm)	Vein Surface Topography	BMF Viscosity (mPa*s)	Min WSS (mPa)	Max WSS (mPa)	Global Average WSS (mPa)	WSS Median (mPa)	Mean Frames per Flow Video	Average WSS CV (%)	Average ROI Wall Coverage (%)
Physiologic	3	Smooth	3.5	34.13	2688.16	255.38 (±54.08)	199.35	99.95	73.98	96.67
Pathologic	6	Smooth	3.5	4.56	479.55	34.52 (±1.36)	29.48	99.95	81.54	96.02
P96 3mo	6.6	Rough	3.5	8.29	431.44	54.11 (±10.32)	43.34	100.00	73.92	89.12
P96 12mo	6.6	Rough	3.5	11.92	561.90	70.76 (±3.26)	53.70	100.00	79.99	88.25
P104 3mo	9	Rough	3.5	3.23	1261.63	35.75 (±3.91)	22.04	99.55	118.61	97.92
P104 12mo	11	Rough	3.5	3.58	1132.31	26.89 (±6.18)	15.94	99.73	161.87	97.15

566

567 **Table 2:** Geometric parameters, BMF viscosity, experimental WSS values (min, max,  
568 global average and median), mean frames per flow video, WSS CV values and ROI wall  
569 coverage values across cephalic arch millifluidic devices under physiologic flow.

570

571

572

573

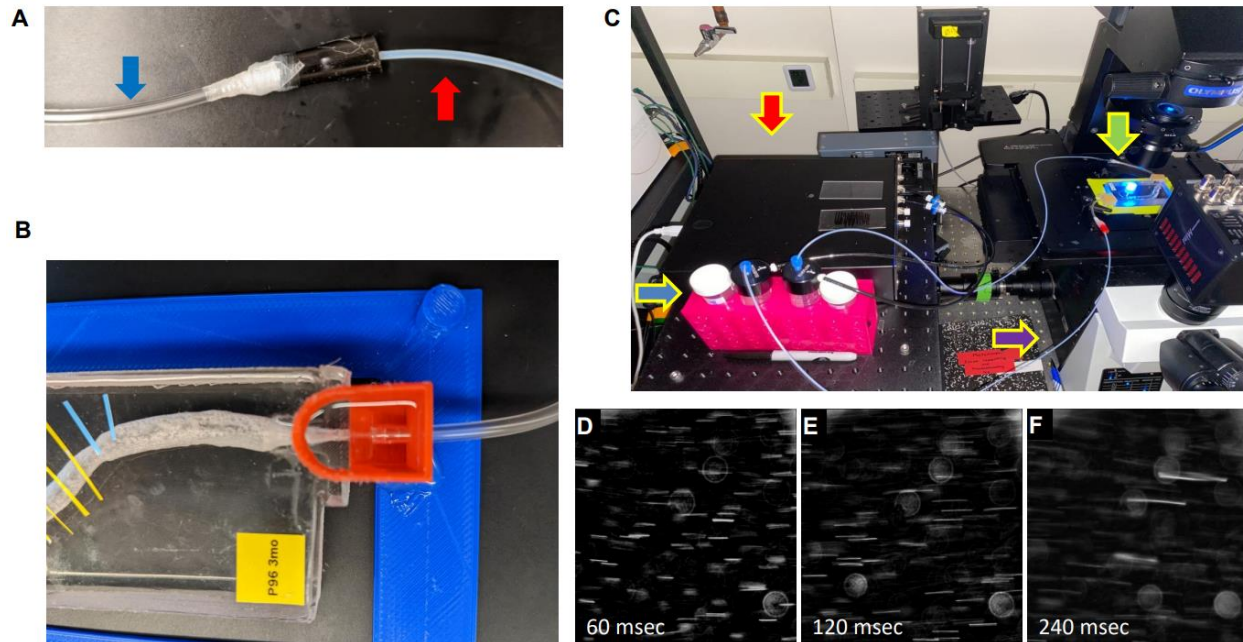
574

575

576

577

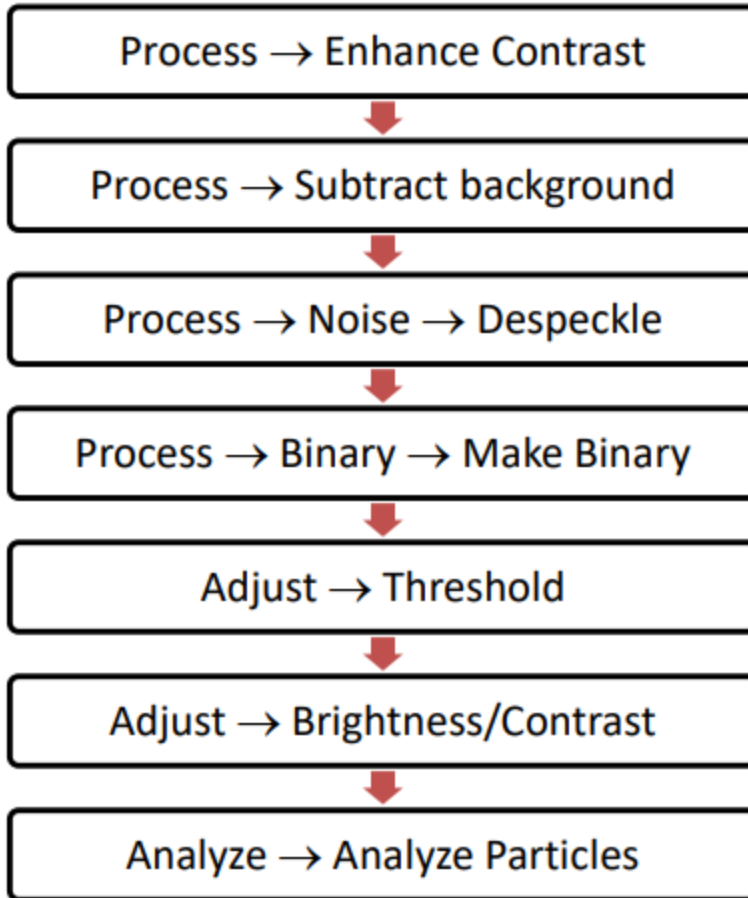
578



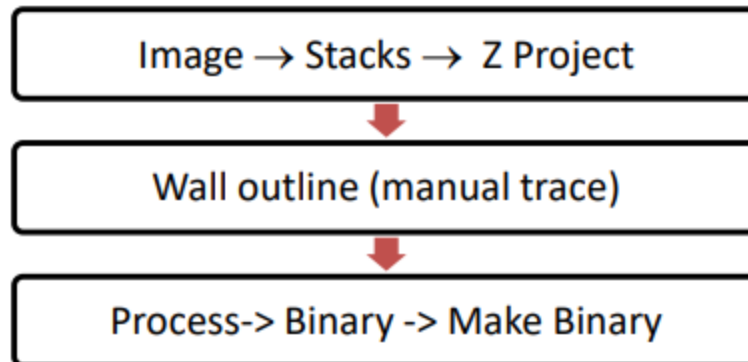
579

580 **Figure S1:** (A) Tubing-tubing junction showing the different tubing diameters and  
 581 materials. Tygon tubing (indicated by blue arrow) is connected to the millifluidic device  
 582 while PEEK tubing (indicated by red arrow) is coupled to the BMF reservoirs. (B) Inlet  
 583 adapter close-up showing the tubing-device junction by means of a plastic barbed tube  
 584 fitting encased in PDMS box structure. (C) Experimental setup to image flow experiments.  
 585 Components include: pressure modulator (red arrow) connected to air compressor,  
 586 reservoir (blue arrow) of blood-mimicking fluid with fluorescent tracer beads, millifluidic  
 587 device (green arrow) under flow mounted on microscope stage and epifluorescence  
 588 microscope (purple arrow). (D-F) Sample ROI flow data depicting how increasing  
 589 exposure time (msec) during image acquisition increases streamline length.  
 590 Experimentally, exposure time is adapted to employed flow rates and millifluidic devices  
 591 to yield sufficiently long streamlines for downstream analysis.

**A**



**B**

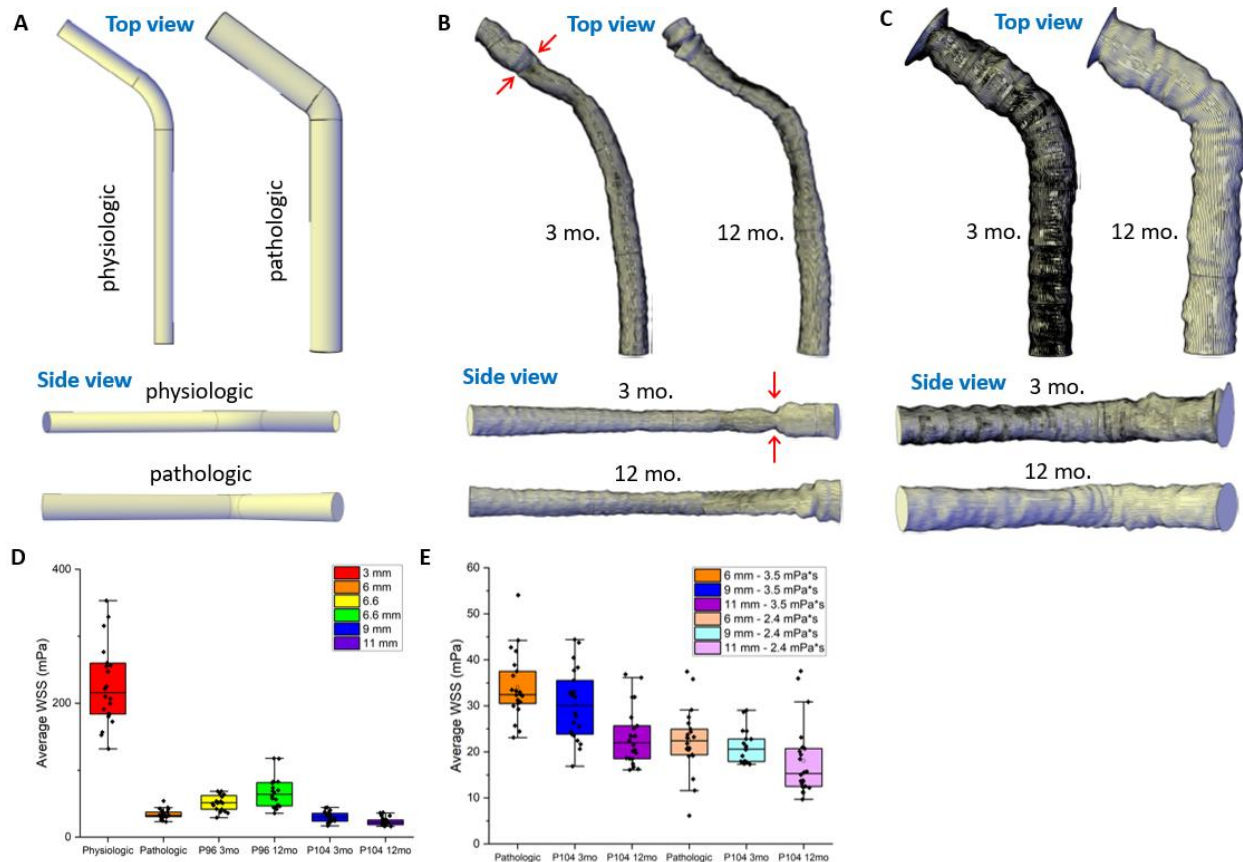


592

593 **Figure S2:** Image preprocessing steps using ImageJ to extract (A) streamlines, and (B)  
594 outline of the vein wall.

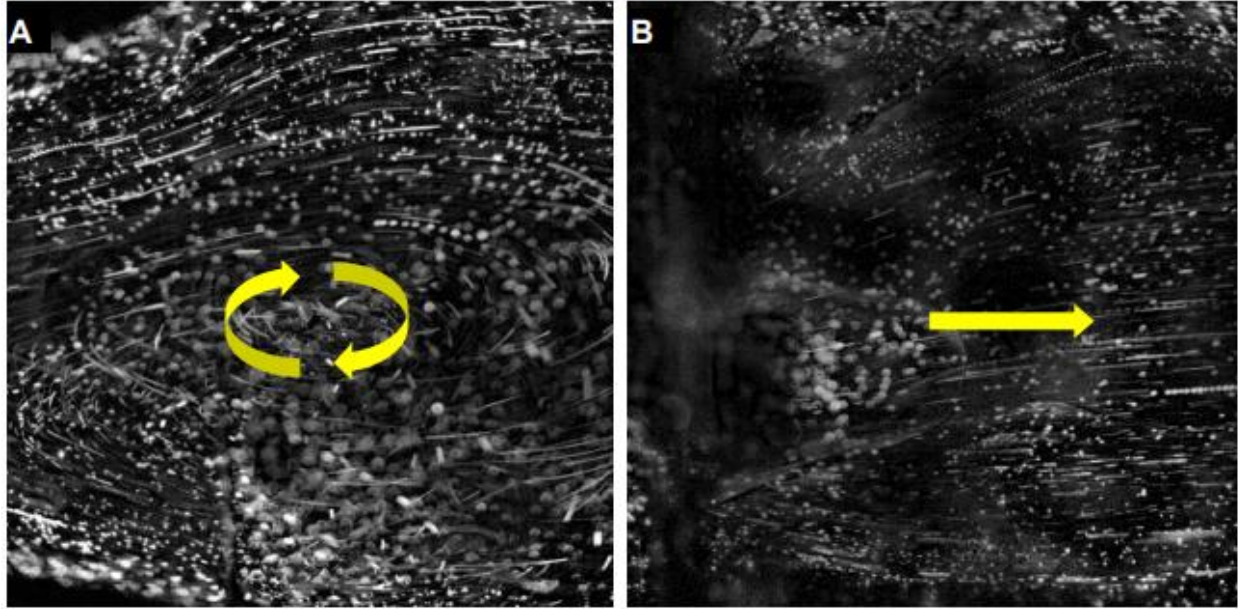
595

596



597

598 **Figure S3:** Top and side views of (A) physiologic and pathologic, (B) P96: 3 and 12 mo.,  
 599 and (C) P104: 3 and 12 mo. cephalic arch models. Red arrows in (B) in P96, 3 mo. model  
 600 highlight a constriction in the postbend region. Patient-to-patient geometric heterogeneity  
 601 and evolution is depicted across time. (D) Average WSS box plot across all models and  
 602 their respective ROIs, average vein diameters shown on legend. Flow data collected  
 603 using BMF with viscosity of 3.5 mPa\*s under physiologic flow. (E) Average WSS plot for  
 604 pathologic and P104 cephalic arch models under physiologic flow using BMF of varying  
 605 viscosity (2.4 and 3.5 mPa\*s). Average vein diameters and viscosities are shown in  
 606 legend.



607

608 **Figure S4:** Images comparing the effect of narrow and wide inlet tubing diameter on flow  
609 at the prebend regions of millifluidic devices under physiologic flow condition. (A) Narrow  
610 tubing causes an eddy (yellow arrows indicate the direction of flow) extending up to a  
611 small portion of the prebend region. (B) Laminar flow (yellow arrow indicates the direction  
612 of flow) in the prebend region of the millifluidic device is achieved by increasing inlet tubing  
613 diameter and improving tubing-device connection. The images are constructed from  
614 videos of tracer beads in the prebend region.

615

616

617

618

619 **References**

- 620 1. United States Renal Data System. 2018 USRDS annual data report: Epidemiology of  
621 kidney disease in the United States. National Institutes of Health, National Institute of Diabetes  
622 and Digestive and Kidney Diseases, Bethesda, MD, 2018. 2018.
- 623 2. Pisoni RL, Zepel L, Fluck R, Lok CE, Kawanishi H, Süleymanlar G, et al. International  
624 Differences in the Location and Use of Arteriovenous Accesses Created for Hemodialysis:  
625 Results From the Dialysis Outcomes and Practice Patterns Study (DOPPS). *American Journal of*  
626 *Kidney Diseases*. 2018;71(4):469-78. doi: <https://doi.org/10.1053/j.ajkd.2017.09.012>.
- 627 3. Casserly LF, Dember LM. Thrombosis in End-Stage Renal Disease. *Seminars in Dialysis*.  
628 2003;16(3):245-56. doi: 10.1046/j.1525-139X.2003.16048.x.
- 629 4. Quencer KB, Oklu R. Hemodialysis access thrombosis. *Cardiovasc Diagn Ther*.  
630 2017;7(Suppl 3):S299-S308. doi: 10.21037/cdt.2017.09.08. PubMed PMID: 29399534.
- 631 5. Thamer M, Lee TC, Wasse H, Glickman MH, Qian J, Gottlieb D, et al. Medicare Costs  
632 Associated With Arteriovenous Fistulas Among US Hemodialysis Patients. *American Journal of*  
633 *Kidney Diseases*. 2018;72(1):10-8. doi: 10.1053/j.ajkd.2018.01.034.
- 634 6. Kaufman JS. Antithrombotic Agents and the Prevention of Access Thrombosis.  
635 2000;13(1):40-6. doi: 10.1046/j.1525-139x.2000.00012.x.
- 636 7. Dember LM, Beck GJ, Allon M, Delmez JA, Dixon BS, Greenberg A, et al. Effect of  
637 Clopidogrel on Early Failure of Arteriovenous Fistulas for Hemodialysis: A Randomized  
638 Controlled Trial. *JAMA*. 2008;299(18):2164-71. doi: 10.1001/jama.299.18.2164 %J JAMA.
- 639 8. Hammes M, Boghosian M, Cassel K, Watson S, Funaki B, Doshi T, et al. Increased inlet  
640 blood flow velocity predicts low wall shear stress in the cephalic arch of patients with  
641 brachiocephalic fistula access. *PLoS One*. 2016;11(4). doi: 10.1371/journal.pone.0152873.
- 642 9. Hammes M, Cassel K, Boghosian M, Watson S, Funaki B, Coe F. A cohort study showing  
643 correspondence of low wall shear stress and cephalic arch stenosis in brachiocephalic  
644 arteriovenous fistula access. *The Journal of Vascular Access*. 2020;22(3):380-7. doi:  
645 10.1177/1129729820942048.
- 646 10. Boghosian M, Cassel K, Hammes M, Funaki B, Kim S, Qian X, et al. Hemodynamics in the  
647 cephalic arch of a brachiocephalic fistula. *Medical Engineering and Physics*. 2014;36(7):822-30.  
648 doi: 10.1016/j.medengphy.2014.03.001.
- 649 11. Sigovan M, Rayz V, Gasper W, Alley HF, Owens CD, Saloner D. Vascular remodeling in  
650 autogenous arterio-venous fistulas by MRI and CFD. *Annals of Biomedical Engineering*.  
651 2013;41(4):657-68. doi: 10.1007/s10439-012-0703-4.
- 652 12. Ene-lordache B, Remuzzi A. Disturbed flow in radial-cephalic arteriovenous fistulae for  
653 haemodialysis: Low and oscillating shear stress locates the sites of stenosis. *Nephrology Dialysis*  
654 *Transplantation*. 2012;27(1):358-68. doi: 10.1093/ndt/gfr342.
- 655 13. Hammes M, Moya-Rodriguez A, Bernstein C, Nathan S, Navuluri R, Basu A.  
656 Computational modeling of the cephalic arch predicts hemodynamic profiles in patients with  
657 brachiocephalic fistula access receiving hemodialysis. *PLoS One*. 2021;16(7 July). doi:  
658 10.1371/journal.pone.0254016.
- 659 14. Hammes M. Importance of the Endothelium in Arteriovenous Fistula Outcomes.  
660 *American Journal of Nephrology*. 2016;44(6):426-7. doi: 10.1159/000452429.

- 661 15. Hammes M, McGill RL, Basu A, Blicharski T, Delaney K. Hemodynamic effects of  
662 hemodialyzer pump speed on arteriovenous fistulas. *Clinical Nephrology*. 2019;91 (2019) -  
663 March (138 - 146)(0301-0430 (Print)). doi: 10.5414/CN109456.
- 664 16. Irfan H, Ooi GS, Kyin MM, Ho P. Revealing Maximal Diameter of Upper Limb Superficial  
665 Vein with an Elevated Environmental Temperature. *International Journal of Chronic Diseases*.  
666 2016;2016:8096473. doi: 10.1155/2016/8096473.
- 667 17. Schneider CA, Rasband WS, Eliceiri KW. NIH Image to ImageJ: 25 years of Image Analysis  
668 HHS Public Access. 2012.
- 669 18. Albayrak R, Yuksel S, Colbay M, Degirmenci B, Acarturk G, Haktanir A, et al.  
670 Hemodynamic changes in the cephalic vein of patients with hemodialysis arteriovenous fistula.  
671 *Journal of Clinical Ultrasound*. 2007;35(3):133-7. doi: 10.1002/jcu.20307.
- 672 19. Bolelli F, Allegretti S, Baraldi L, Grana C. Spaghetti Labeling: Directed Acyclic Graphs for  
673 Block-Based Connected Components Labeling. *IEEE Transactions on Image Processing*.  
674 2020;29(1):1999-2012. doi: 10.1109/TIP.2019.2946979.
- 675 20. Bradski G. The OpenCV Library. *Dr Dobb's Journal of Software Tools*. 2000. PubMed  
676 PMID: opencv\_library.
- 677 21. Baskurt OK, Meiselman HJ. Blood rheology and hemodynamics. *Semin Thromb Hemost*.  
678 2003;29(5):435-50. Epub 2003/11/25. doi: 10.1055/s-2003-44551. PubMed PMID: 14631543.
- 679 22. Boghosian ME, Hammes MS, Cassel KW, Akherat SMJ, Coe F. Restoration of wall shear  
680 stress in the cephalic vein during extreme hemodynamics. *Journal of Medical Engineering and*  
681 *Technology*. 2018;42(8):617-27. doi: 10.1080/03091902.2019.1591534.
- 682 23. Van Tricht I, De Wachter D, Tordoir J, Verdonck P. Hemodynamics and Complications  
683 Encountered with Arteriovenous Fistulas and Grafts as Vascular Access for Hemodialysis: A  
684 Review. *Annals of Biomedical Engineering*. 2005;33(9):1142-57. doi: 10.1007/s10439-005-5367-  
685 X.
- 686 24. Browne LD, Bashar K, Griffin P, Kavanagh EG, Walsh SR, Walsh MT. The Role of Shear  
687 Stress in Arteriovenous Fistula Maturation and Failure: A Systematic Review. *PLoS One*.  
688 2016;10(12):e0145795. doi: 10.1371/journal.pone.0145795.
- 689 25. Dhar P, Eadon M, Hallak P, Munoz RA, Hammes M. Whole blood viscosity: Effect of  
690 hemodialysis treatment and implications for access patency and vascular disease. *Clinical*  
691 *Hemorheology and Microcirculation*. 2012;51:265-75. doi: 10.3233/CH-2012-1532.
- 692 26. Shirazian S, Rios-Rojas L, Drakakis J, Dikkala S, Dutka P, Duey M, et al. The effect of  
693 hemodialysis ultrafiltration on changes in whole blood viscosity. *Hemodialysis International*.  
694 2012;16(3):342-50. doi: <https://doi.org/10.1111/j.1542-4758.2012.00671.x>.
- 695 27. Jain A, van der Meer AD, Papa AL, Barrile R, Lai A, Schlechter BL, et al. Assessment of  
696 whole blood thrombosis in a microfluidic device lined by fixed human endothelium. *Biomedical*  
697 *Microdevices*. 2016;18(4). doi: 10.1007/s10544-016-0095-6.
- 698 28. Rios DRA, Carvalho MG, Figueiredo RC, Ferreira CN, Rodrigues VL, Souza RA, et al.  
699 ADAMTS13 and von Willebrand factor in patients undergoing hemodialysis. *Journal of*  
700 *Thrombosis and Thrombolysis*. 2012;34(1):73-8. doi: 10.1007/s11239-012-0682-1.
- 701 29. Zawaski S, Hammes M, Balasubramanian V. Alternatively Spliced Human Tissue Factor  
702 and Thrombotic Tendencies in Hemodialysis Patients. 2010.
- 703 30. Pequeriaux NC, Fijnheer R, Gemen EF, Barendrecht AD, Dekker FW, Krediet RT, et al.  
704 Plasma concentration of von Willebrand factor predicts mortality in patients on chronic renal

705 replacement therapy. *Nephrol Dial Transplant*. 2012;27(6):2452-7. Epub 2011/12/23. doi:  
706 10.1093/ndt/gfr735. PubMed PMID: 22189209.  
707